1   **Integration of microseism, wavemeter buoy, HF Radar and hindcast data to analyze the**

2   **Mediterranean cyclone Helios**

4   **Alfio Marco Borzì[1*], Vittorio Minio[1], Raphael De Plaen[2], Thomas Lecocq[2], Salvatore**

5   **Alparone[3], Salvatore Aronica[4], Flavio Cannavò[3], Fulvio Capodici[5], Giuseppe Ciraolo[5],**

6   **Sebastiano D'Amico[6], Danilo Contrafatto[3], Giuseppe Di Grazia[3], Ignazio Fontana[4],**

7   **Giovanni Giacalone[4], Graziano Larocca[3], Carlo Lo Re[7], Giorgio Manno[5], Gabriele**

8   **Nardone[7], Arianna Orasi[7], Marco Picone[7], Giovanni Scicchitano[8], Andrea Cannata[1,3]**

9   [1]Dipartimento di Scienze Biologiche, Geologiche ed Ambientali - Sezione di Scienze della Terra, Università degli
10   Studi di Catania, Catania, Italy;

11   [2]Seismology-Gravimetry, Royal Observatory of Belgium, Brussel, Belgium;

12   [3]Istituto Nazionale di Geofisica e Vulcanologia - Sezione di Catania, Osservatorio Etneo, Catania, Italy;

13   [4]Institute of Anthropic Impacts and Sustainability in the Marine Environment - National Research Council (IAS-
14   CNR), Campobello di Mazara, TP, Italy

15   [5]Dipartimento di Ingegneria Civile, Ambientale, Aerospaziale, dei Materiali, University of Palermo, 90128
16   Palermo, Italy

17   [6]Department of Geosciences, University of Malta, Msida, Malta;

18   [7]Centro Nazionale per la Caratterizzazione Ambientale e la Protezione Della Fascia Costiera, la Climatologia
19   Marina e l'Oceanografia Operativa, Italian National Institute for Environmental Protection and Research, Rome,
20   Italy.

21   [8]Dipartimento di Scienze della Terra e Geoambientali, Università degli Studi di Bari Aldo Moro, 70125 Bari, Italy

22   *Corresponding author

23   alfio.borzi@phd.unict.it

24   Corso Italia 57, 95129 Catania (Italy)

26   **Keywords:** Microseism, wavemeter buoy, HF Radar, Mediterranean cyclones, climate change,

27   monitoring sea state

28   **Abstract**

29   In this work, we study a Mediterranean cyclone, that was called Helios and took place during

30   the period 9-11 February 2023 in the southeastern part of Sicily and Malta Island, by a

31   multiparametric approach combining microseism results with sea state and meteorological data

32   provided by wavemeter buoy, HF Radar, hindcast maps and satellite SEVIRI images. The sub-

33   tropical system Helios caused heavy rainfall, strong wind gusts and violent storm surges with

34   significant wave heights greater than 5 meters. We deal with the relationships between such a

35   system and the features of microseism (the most continuous and ubiquitous seismic signal on

36   the Earth) in terms of spectral content, space-time variation of the amplitude and source

37   locations tracked by means of two different methods (amplitude-based grid search and array

38   techniques). By comparing the location of the microseism sources and the area affected by

39   significant storm surges, derived from sea state data, we note that the microseism location

40   results are in agreement with the real position of the storm surges. In addition, we are able to

41   obtain the seismic signature of Helios using a method that exploits the coherence of continuous

42   seismic noise. Hence, we show how an innovative monitoring system of the Mediterranean

43   cyclones can be designed by integrating microseism information with other techniques

44   routinely used to study meteorological phenomena.

46   **1. Introduction**

47   Significant storm surges driven by intense low-pressure systems represent one of the main

48   hazards to the Mediterranean coastal areas causing flooding, beach erosion and damage to

49   infrastructures and cultural heritages (Flaounas et al., 2022; Lionello et al., 2019;).

50   Occasionally, when there are favorable conditions like high sea temperature and high contrast

51 of temperature sea-air, the cyclones can acquire the characteristics of a MEDIterranean

52 hurriCANE (hereinafter Medicane). Medicanes genesis is favored when an extratropical

53 depression gets isolated from the polar jet stream. The "cut-off" feature, when situated above

54 the Mediterranean Sea, remains relatively stable and takes advantage of the abundant heat and

55 humidity from the sea to generate organized convection (Faranda et al., 2022).

56 The structure of a Medicane is characterized by the presence of a central free-cloud "eye", a

57 strong rotation around the pressure minimum, an eyewall with convective cells, from which

58 rain bands extend. It can be considered like a small-scale tropical cyclone and can lead to sea-

59 level rise, storm surge and sea waves that can reach significant heights of about five meters

60 (Miglietta and Rotunno, 2019). The typical Medicane lifetime is limited to a few days,

61 generally from 2 to 5 days, as a result of the small areal extension of the Mediterranean Sea

62 that represents their main energy source; for the same reason also the diameter is generally

63 restricted to a range between 100 and 300 km (Comellas et al., 2021), and their intensity rarely

64 exceeds the category 1 of the Saffir-Simpson hurricane wind scale (Miglietta end Rotunno.,

65 2019). In addition, due to the geometrical and meteorological characteristics of the

66 Mediterranean Sea, a Medicane reaches fully tropical characteristics (a symmetric, deep warm-

67 core structure and convection in their development and maintenance) for a short time, while

68 extratropical features (non-symmetrical structure and not well-developed convection around

69 the core) prevail for most of their lifetime (Miglietta et al., 2011, 2013). There is no clear

70 separation between tropical and extratropical cyclones, the first approach to differentiate these

71 cyclones was developed by Hart (2003). This method, called cyclone phase space analysis,

72 relies on a large spectrum of different cyclone types in a way to form a continuum between

73 tropical and extratropical cyclones.

74 The favorable months to the Medicanes generations are the autumn and early winter months

75 (from September to January). Indeed during these months, the Mediterranean Sea preserves

76   high temperatures after the summer season, and the first cold upper-air troughs are observed,

77   thus creating a high sea-air temperature gradient (Cavicchia et al., 2014; Nastos et al., 2018).

78   Specifically, the occurrence of intense convective instability is initiated when the polar jet

79   stream transports cold air masses over the warmer Mediterranean Sea (Cavicchia et al., 2014;

80   Nastos et al., 2018). The Medicanes generation during the late-winter months (February and

81   March) is possible but less common (Cavicchia et al., 2014, Tous and Romero, 2013).

82   These Mediterranean extreme weather events caused damages, floods, deaths, and injuries in

83   several Mediterranean coastal areas (South France, Central and South Italy, Malta, Balearic

84   islands, Greece, Crete, Turkey, and some African states; Androulidakis et al, 2022; Bouin and

85   Brossier, 2020; Carrió et al., 2017; Dafis et al., 2018; Di Muzio et al., 2019; Faranda et al.,

86   2022; Kerkmann and Bachmeier, 2011; Lagouvardos et al., 2022; Pravia-Sarabia et al., 2021;

87   Portmann et al., 2020; Rumora et al., 2018; Varlas et al., 2020; Zimbo et al., 2022). As

88   explained by Cavicchia et al. (2014), the most frequent genesis regions are the Balearic Islands

89   and the Ionian Sea. In particular, during the last 12 years, the majority of the Medicanes have

90   been developed over the Ionian Sea and this is probably linked to the sea surface temperature

91   that, as shown by Shaltout and Omstedt (2014), in the Ionian Sea is constantly 1.0°-1.5° C

92   higher than that in the Tyrrhenian Sea.

93   Although these extreme Mediterranean events showed significant wave heights (hereinafter

94   SWH, defined as the average wave height of the highest one-third of the waves), comparable

95   to the common seasonal storms, they caused greater coastal flooding (Scardino et al., 2022;

96   Scicchitano et al., 2021). The strong winds, generated during a Medicane, cause the

97   development of powerful wave motions and lead to an energy transfer from the sea waves to

98   the solid Earth (Borzì et al., 2022). This energy transfer between the atmosphere, the

99   hydrosphere and the solid Earth is one of the generation mechanisms of the most continuous

100   and ubiquitous seismic signal on the Earth, called microseism (e.g. Hasselmann, 1963;

101   Longuet-Higgins, 1950). In connection with the spectral content and the source mechanism

102   (e.g. Haubrich and McCamy, 1969), it is possible to divide this signal into: primary microseism

103   (PM), that shows the same period as the oceanic waves (13 - 20 s) and low amplitudes, and is

104   generated by the energy transfer of oceanic waves breaking against the shoreline (Ardhuin et

105   al., 2015; Hasselmann, 1963); secondary microseism (SM), generated by sea waves with the

106   same frequency traveling in opposite directions and exhibiting frequency about twice of the

107   frequency of the oceanic waves (period of 5 - 10 s) and amplitude higher than the PM (e.g.

108   Ardhuin and Roland, 2012; Ardhuin et al., 2015; Longuet-Higgins, 1950; Oliver and Page,

109   1963); short-period secondary microseism (SPSM), that has a period shorter than 5 seconds

110   and is generated by the interaction between local wave motions near the coastline (Bromirski

111   et al., 2005).

112   Several works deal with the relationship between microseism and the sea state (Ardhuin et al.,

113   2019; Cannata et al., 2020; Guerin et al., 2022; Moschella et al., 2020), while others take into

114   account specifically the relationship between microseism and cyclonic activity (e.g.,

115   Bromirski, 2001; Bromirski et al., 2005; Gerstoft et al., 2006; Gualtieri et al., 2018; Lin et al.,

116   2017; Retailleau and Gualtieri, 2019, 2021; Zhang et al., 2010) considering in particular

117   typhoons (Lin et al., 2017), tropical cyclones (Zhang et al., 2010), and hurricanes (Gerstoft et

118   al., 2006). Interestingly, Bromirski (2001) and Bromirski et al. (2005) showed that the

119   microseism bands most affected by the presence of a cyclone are the SM and SPSM ones.

120   For the first time, the relationship between SM, SPSM, and Medicane was analyzed by Borzì

121   et al. (2022), who considered the Medicane Apollo to reconstruct both the seismic variation in

122   terms power spectral density (PSD) and root mean square (RMS) amplitude and the Medicane

123   position during its lifetime by two different methods (array analysis and grid search method by

124   means of seismic amplitude decay). In this work, we explore the relationship between

125   microseism and the Sub-Tropical system "Helios" that occurred in the Sicily Channel during

126   the period 9-11 February 2023 (**Figure 1**). The microseism results are integrated with

127   wavemeter buoy, HF Radar, hindcast and satellite data (SEVIRI Images) to perform an

128   investigation as comprehensive as possible of this extreme Mediterranean meteo-marine event.

129   **2. Sub-tropical system "Helios" (9-11 February 2023)**

130   During the period 9-11 February 2023, a low-pressure system, later renamed Helios, developed

131   over the Sicily Channel due to the strong contrast between the very cold air, coming from NE

132   (Balkans area) and the relatively warm sea surface. From satellite data, the warm core anomaly

133   of this cyclone is evident, requisite for the development of the Medicane. However, this storm

134   failed to become a Medicane, for which it is necessary that the cyclone maintains well-

135   developed convection around the eye, absent in this case probably due to a little interaction

136   between sea-air caused by sea surface temperature not suitable for the development of a

137   Medicane   (https://twitter.com/medcyclones/status/1623795373423620096?s=20,

138   https://twitter.com/medcyclones/status/1623992335104081921?s=20,

139   https://twitter.com/medcyclones/status/1624143740800536591?s=20, last access 23/05/2023).

140   In spite of this, Helios, thanks to its proximity to the Sicilian and Maltese coasts, was able to

141   produce damage along these areas. The effects of the sub-tropical system Helios were

142   significant, especially in Catania, Ragusa and Siracusa provinces (located in the south-eastern

143   part of Sicily), where the Sicilian Meteorological service ("Regione Siciliana—SIAS—

144   Servizio Informativo Agrometeorologico Siciliano", http://www.sias.regione.sicilia.it/)

145   recorded heavy rainfall, more than 200 mm/48 h and peaks of about 500 mm/48 h near Noto

146   for the days 9-10 February 2023, heavy snowfall starting from 1200 m a.s.l. with accumulations

147   of fresh snow on Etna thicker than two meters, strong wind gusts up to 90 km/h along the

148   exposed coast (Davies, 2023) and severe storm surge with SWH greater than 5 meters. Similar

149   effects were also recorded in Malta. The minimum pressure value in the cyclone eye amounted

150   to 1002 hPa. An overview of the positions and the extension of the sub-tropical system Helios

151   is represented in **Figure 1.**

152   As a consequence of the damage caused by Helios, the Regional Sicilian Government decided

153   to require a national state of emergency for 12 months for all the municipalities of Catania,

154   Siracusa, and Ragusa provinces and some municipalities of Messina province

155   (https://www2.regione.sicilia.it/deliberegiunta/file/giunta/allegati/N.099_15.02.2023.pdf, last

156   access 23/05/2023).

157

158   **3. Data and Methods**

159   We analyzed the data recorded in the period 8 to 13 February 2023 comprising the development

160   of Helios, the climax in terms of minimum pressure value, wind velocity, precipitation intensity

161   and SWH, and its decline.

162   **3.1. Seismic data**

163   We used 105 seismic stations installed along the Italian and French coastal areas, in the Sicily

164   channel coastlines (in Malta, Lampedusa and Linosa islands), in Corsica island and along the

165   Greek coastal areas to perform spectral analysis, localization analysis by the grid search method

166   based on seismic amplitude decay and to obtain the seismic signature of the analyzed event

167   (**Figure 2a** and **Supplementary Table 1**). Additionally, 15 seismic stations, installed in the

168   Etnean area, were used to conduct array analysis (**Figure 2b** and **Supplementary table 2**). The

169   selected seismic stations show specific characteristics: they are i) installed near the coastal

170   areas and ii) equipped with 3-component broadband seismic sensors.

171   **3.2. Sea state measures**

172   In this work, we use sea state data derived from four independent methodologies. In particular,

173   we used: i) significant wave height (SWH-Hind), provided by the hindcast maps produced by

174   Copernicus; ii) significant wave height (SWH-Buoy), period and direction of the waves

175   measured by the wavemeter buoy installed near Mazara del Vallo; iii) significant wave height

176   (SWH-HF), period and direction of the waves obtained by the HF Radar installed at the Marina

177   di Ragusa harbor; iv) SEVIRI Images to spatially and temporally track the position of the

178   cyclone. These four different data sources have been used to both describe the sea state

179   evolution during the Helios event, and characterize the physical state of the sea which is strictly

180   correlated to the microseism derived outputs.

181   **3.2.1. Copernicus Data**

182   Regarding the description of the Helios event in terms of spatio/temporal distribution of SWH,

183   wave   period   and   direction   over   the   whole   domain,   we   referred   to   the

184   "MEDSEA_HINDCAST_WAV_006_012" product, provided by the Copernicus Marine

185   Environment Monitoring Service (CMEMS) (Korres et al., 2019). The CMEMS product

186   contains the hindcast maps of the Mediterranean Sea Waves forecasting system and is based

187   on the third-generation wave model WAM Cycle 4.5.4 composed by hourly wave parameters

188   at 1/24° horizontal resolution (Korres et al., 2019).

189   **3.2.2 Wavemeter buoy data**

190   Concerning the wave buoy, in **Figure 2c** we show the locations of this buoy, located offshore

191   of Mazara del Vallo, at a depth of 85 m. The Mazara buoy is managed by ISPRA and is part of

192   the National Wave Buoy Network (RON). The instrumental equipment consists of buoys

193   allowing the acquisition of wave parameters in real time. The long time series represent an

194   important heritage for the knowledge of marine phenomena affecting the Italian seas, both in

195   terms of climatology and extreme events. The RON National Wave Network is now composed

196   of 7 stations located off the Italian coasts for the continuous measurement of wave and

197   meteorological parameters, such as wind direction and speed, atmospheric pressure, water

198   surface and air temperatures, with real-time data transmission. Until 2014, the ISPRA wave

199   buoy network was equipped with WatchKeeper™ weather wave meters manufactured by the

200   Canadian company AXYS Ltd. (Bencivenga et al., 2012). The new meteo-marine buoys were

201   developed, designed and built in Italy for the specific needs of ISPRA. Data are collected

202   continuously for periods of 20-25 minutes and are provided every 30 minutes.

203   The parameters recorded by the wavemeter buoy and used in this study are: i) SWH (m), ii)

204   wave mean period (s) and iii) wave mean direction (°).

3.2.3. HF Radar data

206   Sea state measures are also provided by the HF system located in the Marina di Ragusa harbor

207   (**Figure 2c**) which is owned by the CNR-IAS (Consiglio Nazionale delle Ricerche - Istituto

208   per lo Studio degli Impatti Antropici e Sostenibilità in Ambiente Marino). This HF radar is part

209   of the CALYPSO HF network operating in the Malta-Sicily channel since 2013. The network

210   is nowadays composed of seven HF Codar SeaSonde systems transmitting at 13.5 MHz (central

211   frequency). The network provides sea surface current maps at 3 km of spatial resolution at

212   hourly scale (Capodici et al., 2019). Each HF radar provides sea state variables (SWH-HF,

213   wave period, wave direction) every 15 minutes; these data are referred to 10 independent

214   annular rings 3 km wide, centered at the HF site location. Data used in this work regard the last

215   annular ring (30 km far from the HF site) showing the best temporal continuity of the

216   measurements. The sea state derived by the HF technology has been deeply validated by several

217   authors (e.g. Long et al., 2011; Lorente et al., 2021; Orasi et al., 2019; Saviano et al., 2019).

3.2.4. Satellite data

219   The passage of the Helios cyclone in the study area was tracked by means of the High Rate

220   SEVIRI Level 1.5 Image Data. The Level 1.5 image data represents the geolocated and

221   radiometrically pre-processed images that are prepared for subsequent processing steps, e.g.

222   the extraction of meteorological products helpful in our case study. For further information

223   about   this   methodology   you   can   see   the   EUMETSAT   website

224   (https://navigator.eumetsat.int/product/EO:EUM:DAT:MSG:HRSEVIRI   last   access

225   25/05/2023). In particular, an image at 10.8 μm each 15' was downloaded and analyzed.

226   The above mentioned measures allowed describing the spatial and temporal characteristics of

227   the sea state during the Helios event, that were compared to the features of the microseism.

228   **3.3. Spectral Analysis of Microseism**

229   The seismic data were corrected for the instrument response and thereafter spectral and

230   amplitude analyses were performed. For the spectral analysis, hourly spectra of the seismic

231   signal were calculated by applying Welch's method (Welch, 1967) with time windows of 81.92

232   s. The hourly spectra, thus obtained, were gathered and represented as spectrograms, with time

233   on the x-axis, frequency on the y-axis, and the $\log_{10}$ of the PSD indicated by a color scale.

234   Some spectrograms obtained from the vertical component of 4 stations are shown in **Figure 3**.

235   Concerning the amplitude, we estimated hourly RMS amplitude time series for the typical

236   microseism frequency bands: 0.2-0.4 Hz (SPSM, **Supplementary Figure 1**), 0.1-0.2 Hz (SM,

237   **Figure 3**) and 0.05-0.07 Hz (PM, **Supplementary Figure 2**).

238   In addition, to show the spatial and temporal distribution of the RMS amplitude during the

239   period under investigation, we plotted the mean RMS amplitude computed on non-overlapped

240   1-day-long moving windows for the three microseism bands. Each dot, in **Figure 4,** represents

241   a seismic station and the color of the dot relates to the corresponding RMS amplitude at that

242   location, as specified in the color bar. Noteworthy, the colorbar of the PM band

243   **(Supplementary Figure 3)** shows a different range of RMS amplitude highlighting a different

244   response between the PM and the SM and SPSM bands to the sub-tropical system Helios

245   (**Figure 4** and **Supplementary Figure 4**). Furthermore, in this case, we compared the RMS

246   amplitude with the SWH, represented by the contour lines.

247   **3.4. Tracking Helios position by Microseism**

248   Following Borzì et al. (2022), we used two different and complementary methods to track the

249   position of the sub-tropical system Helios from a seismic point of view. In particular, we use

250   i) a grid search method based on the seismic amplitude decay and ii) array analysis. These

251   methods allow us to track the evolution over time of the location of the centroid of the seismic

252   sources generated by the sea state variations induced by the cyclone. Such seismic data were

253   compared with the cyclone trajectory which was identified by processing the High Rate MSG

254   SEVIRI images. This latter task was accomplished by visually identifying the positions of the

255   cyclone's eye which was clearly identifiable only between 01:00 and 23:00 of the 10 February

256   2023.

257   **3.4.1. Grid search method**

258   We used the seismic signals recorded by 105 seismic stations (**Figure 2a**) to map out the

259   position of Helios during the analyzed period by employing a grid search approach (**Figure 5**).

260   The region, where we executed the grid search, is a bi-dimensional area of 1760 km x 2400 km

261   (minimum longitude: 5°; maximum longitude: 30°; minimum latitude: 30°; maximum latitude:

262   46°) with a spacing of 1°. As shown by several authors who used seismic amplitude decay

263   methods, both to locate microseism sources (Borzì et al. 2022) and seismo-volcanic sources

264   (Battaglia and Aki, 2003; Cannata et al., 2013; Kumagai et al., 2011), the grid spacing is chosen

265   as a compromise between good spatial resolution and reasonable computation time. The

266   microseism source is localized based on the goodness of the linear regression fit (hereafter

267   referred to as R^2) computed for each node of the bi-dimensional (2D) grid previously

268   mentioned. Specifically, the source was identified at the centroid position of all the grid nodes

269   where the R2 values deviate by no more than 1% from the maximum R2 value. In this method,

270   we used an RMS signal window of 4 hours and thus we were able to obtain 1 localization every

271   4 hours. In addition, following Borzì et al. (2022), we applied a method to evaluate the

272   statistical significance of the retrieved maximum R^2 value and to test the confidence of the

273   location results. Specifically, we conducted 20 iterations by randomly rearranging the RMS

274   amplitude values among the stations. Then, we calculated the 95th percentile and we obtained

275   a value of 0.27. In accordance with this result, we consider reliable the localizations with R^2

276   values greater than 0.27.

277   It must be underlined that the grid search method used in this study shows various limits that

278   in specific cases can invalidate the source locations. In particular, the first limit concerns the

279   fact that in this method we consider the microseism source as a point-like source, while the

280   microseism is produced in a wide area of the Mediterranean Sea. In this scenario, the

281   localization of the point-like source is determined as the barycentric point of the extended

282   source. However, it is important to consider a limitation of this method related to the presence

283   of multiple sources with similar amplitude in the same frequency range. In such cases, the

284   constrained source location shifts towards a position between the actual seismic source

285   locations (Battaglia et al., 2005), resulting in a significant decrease in R2;. In our case, we

286   neglect localization showing R^2 values smaller than 0.27, to avoid unreliable localization.

287   **3.4.2. Array analysis**

288   In order to track the location of the sub-tropical system Helios using array techniques, we

289   considered fifteen stations belonging to the Mt. Etna seismic permanent network and used them

290   as a roughly circular array (**Figure 2b**).

291   The Array Response function (ARF) is a good tool to plan the array geometry required to

292   investigate microseism signals or, in this case, to evaluate the performance of a pre-existing

293   array in microseism studies. The ARF, previously obtained by Borzì et al. (2022), exhibits that

294   the roughly circular array has a good response for the PM and SM cases.

295   In this study, we employed the f-k (frequency-wavenumber) analysis technique on microseism

296   signals (e.g. Rost and Thomas, 2002). This approach involves a spectral domain beamforming

297   method that utilizes a grid search of slowness to determine the back azimuth and apparent

298   velocity values that maximize the amplitude of the combined array traces. The result of the f-

299   k analysis is the PSD as a function of slowness. In accordance with Borzì et al. (2022), we

300   followed the subsequent processing steps to implement array analysis on microseismic data:

301   (i) demeaning and detrending; (ii) applying a specific frequency band filter for microseism;

302   (iii) segmenting the data into tapered windows of 120 seconds each; (iv) excluding windows

303   containing seismo-volcanic amplitude transients (such as volcano-tectonic earthquakes, long-

304   period events, and very long-period events) identified using the STA/LTA technique (e.g.,

305   Trnkoczy, 2012); (v) performing f-k analysis for each window by conducting a slowness grid

306   search (ranging from -1 to 1 s/km in the east and north components of the slowness vector)

307   with a spacing of 0.05 s/km. An illustrative example of the outcomes is presented in Figure 5.

308   For further details about these two methods used in this work, you can see Borzì et al. (2022).

309   **3.5. Seismic signature of the Medicanes**

310   In a way to obtain the seismic signature and the main spectral characteristics of the sub-tropical

311   system Helios, we use a method developed by Soubestre et al. (2018). This method was initially

312   developed as a network-based method to detect and classify seismo-volcanic tremors. The

313   proposed method utilizes the coherence of tremor signals within the network, which is

314   determined based on the array covariance matrix. Using this technique, as explained by

315   Soubestre et al. (2018), it is possible to highlight both volcanic tremors and other types of

316   seismic sources such as tectonic earthquakes (local, regional, and teleseismic), and oceanic

317 seismic noise (microseism). This method allows the identification of the spatially coherent

318 individual noise source within a specific network, identified as small spectral width, as opposed

319 to other noises such as local effects that would generate multiple individual sources. For further

320 details about the method, see Soubestre et al. (2018).

321 In this study, we are interested in detecting the microseism produced by the sub-tropical system

322 Helios. Since we are interested in such a microseism, we filtered the signal in the band 0.1-1

323 Hz and resample it to 25 Hz in a way to reduce the computation time. To compute the

324 covariance matrix we use only the vertical component of the seismic signal and a window

325 length of 60 seconds. The analyses were performed using the data recorded by a station set

326 comprising both stations installed near the south Sicilian coast (CLTA and IWAV5) and in the

327 Malta (MSDA) and Linosa (LINA) islands in order to have the microseism source within the

328 selected station set.

329

330 **4. Results and Discussion**

331 We analyze the sea state, derived by four independent techniques, and the seismic data recorded

332 by the i) 105 seismic stations represented in **Figure 2a** and by ii) the 15 Etnean seismic stations

333 (**Figure 2b**) during the period 8-13 February 2023. We chose a period longer than the real

334 lifetime of the sub-tropical system Helios in a way to include the development, the climax in

335 terms of meteorological events that occurred during the days 9-10 February, and the following

336 loss of intensity.

337 **4.1. Sea state**

338 In **Figure 6**, we show the SWH, the mean wave period and the direction time series recorded

339 during the period 8-13 February 2023 by the buoy of Mazara del Vallo (**Figure 6b, d and f**)

340 and the HF radar installed in Marina di Ragusa harbor (**Figure 6a, c and e**).

341   The buoy data indicates that the sea storm reached its maximum significant wave height of 3.1

342   m at 20:00 on 9 February, with a mean direction of 140° indicating that waves were generated

343   by Scirocco wind, which is the main wave direction for the period under investigation and a

344   period that varies from 5 to 9 s. The data from HF Radar, installed closer to the cyclone position

345   than the buoy, show a maximum SWH of about 6 m recorded on 9 February at 22:30, the mean

346   wave direction was of 100° approximately and the period varies in the range of 5-12 s. Both

347   datasets allowed defining the time interval of the wave storm which spanned between 8-13

348   February 2023. The higher SWH measured by the HF radar agrees with the shorter distance

349   from the cyclone eye (~90 km) of this instrument compared to that of the wave buoy (~190

350   km).

351   The spatio-temporal distribution of the SWH in the whole area is shown by the hindcast maps

352   in **Figure 7**. Noticeably that the stronger effect of the sub-tropical system Helios on the sea

353   state of the Malta-Sicily channel was the increase of the SWH during 9 - 10 February. On 9

354   February the higher SWH values were recorded mainly in the patch of the sea at the east of

355   Sicily Island and of the Maltese archipelago, whereas the wave storm invaded the whole Malta-

356   Sicily channel on 10 February. Finally, on 11 February the wave storm started moving to the

357   south, reaching the northern part of the African coasts.

358   The comparison between SWH-Hind and SWH-HF revealed a good agreement (R^2~0.85) even

359   if an underestimation of the event by the CMS model (slope of ~0.7) was observed

360   (**Supplementary Figure 5**).

361   **4.2. Spectral Analysis and RMS spatial distribution**

362   To perform the spectral analysis we used the 105 seismic stations installed along the Italian,

363   Greek and Maltese coastal areas. In **Figure 3,** we plot the spectrograms and the RMS amplitude

364   time series, obtained by analyzing the vertical component of the seismic signals recorded by

365   four stations installed in Malta (MSDA **Figure 3a**), on Linosa Island (LINA **Figure 3b**), near

366 Pozzallo (IWAV5 **Figure 3c**) and in Central Italy (CELB **Figure 3d**). We chose these four

367 stations to compare the results obtained from the stations installed near the sub-tropical system

368 (LINA, MSDA and IWAV5), with the result obtained from the far station (CELB).

369 As shown by Borzì et al. (2022), in the spectrograms a great part of the energy is focused in

370 the 0.1-1 Hz band, corresponding with the SM and SPSM bands. In addition, it is also evident

371 how the considered stations show a different behavior, in terms of both spectrograms (**Figure**

372 **3**) and RMS amplitude time series (**Figure 3** and **Supplementary Figures 1** and **2**), that

373 depended on their position. In particular, spectrograms and RMS amplitude time series

374 obtained from the data recorded by MSDA (**Figure 3a** and **Supplementary Figure 1a** and **2a**),

375 LINA (**Figure 3b** and **Supplementary Figures 1b** and **2b**) and IWAV5 (**Figure 3c** and

376 **Supplementary Figures 1c** and **2c**) stations, installed close to Helios (**Figure 1** and **Figure**

377 **2**), show the maximum PSD and RMS amplitude values during the time interval 9-11 February

378 2023, highlighted by the vertical dashed lines in **Figure 3**. On the other hand, the spectrogram

379 and RMS amplitude time series of the station CELB (**Figure 3d** and **Supplementary Figures**

380 **1d** and **2d**), installed in the Tyrrhenian area, exhibited the maximum PSD and RMS amplitude

381 values a few days before Helios at the same time as a local storm surge.

382 To show the space-time distribution of the RMS amplitude, we calculate the daily RMS average

383 for the three main microseism bands (PM and SPSM in **Supplementary Figures 3** and **4**, SM

384 in **Figure 4**) during the period 8-13 February 2023. All the three analyzed microseism bands

385 show a relationship with the position of Helios indicated by the five-pointed red star (**Figure**

386 **4c** and **Supplementary Figures 3c** and **4c**). In particular, on 10 February 2023, when Helios

387 reached its climax, the maps in **Figure 4c** (SM) and **Supplementary Figures 3c** and **4c** (PM

388 and SPSM respectively) show a cluster of high RMS values for the stations installed near the

389 sub-tropical system Helios, highlighting a good match between the SM, SPSM, PM and Helios

390 positions.

391 Comparing the results obtained for the sub-tropical system Helios with the results obtained for

392 the Medicane Apollo (Borzì et al., 2022), we observe a similar trend for the SM and SPSM

393 bands and a different behavior for the PM band. In particular, during the Medicane Apollo, the

394 analysis did not show a significant amplitude increase in the PM band, while during the sub-

395 tropical system Helios, the RMS amplitude time series for the PM (**Supplementary Figure 2**),

396 although with two orders of magnitude smaller, showed a trend similar to the SM (**Figure 3**)

397 and SPSM (**Supplementary Figure 1**) ones. Also the space-time distribution shows a good

398 match between the PM (**Supplementary Figure 3**) and Helios position (**Figure 1**, **4c** and

399 **Supplementary Figures 3c** and **4c**), even if for this band there are stations installed in central

400 Italy that show high RMS amplitude values related to a very local storm surge that occurred at

401 the same time as Helios.

402 The involvement of the PM band in the case of the sub-tropical system Helios can be explained

403 by considering the position of this low-pressure system (**Figure 1**) and comparing it with the

404 Apollo position. Indeed, the Medicane Apollo develops and moves in the Ionian Sea (**Figure**

405 **2**) in an area with a sea depth greater than 2000 m, while the sub-tropical system Helios

406 develops and moves largely in the Sicily Channel, a shallower sea with a depth that reaches a

407 maximum depth of 500 m b.s.l. and an average depth of 316 m b.s.l. In addition, the average

408 depth between Sicily and Malta is about 65 m b.s.l. As outlined in the literature (Bromirski et

409 al., 2005), the production of the PM is hindered in large water depths due to the attenuation of

410 pressure fluctuations, which generate the signal, as a result of depth-dependent amplitude

411 decay. More specifically, the PM is generated solely in depths less than half of the wavelength

412 (where λ represents the wavelength of the oceanic waves generating the pressure fluctuations).

413 If we consider, for the Catania and Mazara areas, a mean waves period of 6.1 and 5.6 s and a

414 peak waves period of 9.7 and 9 s respectively (Agenzia per la Protezione dell'Ambiente e per

415 i Servizi Tecnici Dipartimento Tutela Acque Interne e Marine Servizio Mareografico - Atlante

416   delle onde nei mari italiani), by utilizing the correlation that connects period and wavelength

417   (λ=gT^2/2$\boldsymbol{\pi}$ with g acceleration of gravity that is 9.8 m/s^2 and T the period of the waves;

418   Sarpkaya and Isaacson, 1981) we obtain a wavelength, for this part of the Mediterranean sea,

419   ranging between ∿45 m and ∿150 m. Considering these wavelengths, the shallow depth of the

420   Sicily Channel, especially in the Malta Channel where the average depth is about 65 m b.s.l.,

421   and the fact that the generation of the PM occurs only for depths less than ½ λ (Bromirski et

422   al., 2005), we can remark that the generation of the PM is possible in the Sicily Channel, while

423   can not occur in the Ionian Sea except in limited areas near the coastline. This is evident in our

424   analysis, and in particular in the RMS amplitude time series. Indeed in the sub-tropical system

425   Helios case, which occurred in the Sicily Channel, we can note a similar trend between the

426   three analyzed microseism bands (**Figure 3** and **Supplementary Figures 1** and **2**), while in the

427   case of the Medicane Apollo, that developed in the Ionian Sea (Borzì et al., 2022), we observe

428   an RMS amplitude increase only for the SM and SPSM bands and no significant variations in

429   the PM bands.

430   **4.3. Comparing the RMS amplitude with the SWH**

431   As mentioned before, microseism is a continuous seismic signal linked to the hydrosphere-

432   solid Earth energy transfer and, as demonstrated by several authors (e.g. Ardhuin et al., 2012;

433   Bromirski et al., 1999; Bromirski et al., 2005; Cutroneo et al., 2021; Ferretti et al., 2013, 2018),

434   the amplitude of this signal is strictly related to the sea state and in particular to the SWH. To

435   analyze the relationship between microseism and SWH, we plot in **Figure 8a** the RMS

436   amplitude time series for the station IWAV5 and the SWH time series derived from both HF

437   Radar (SWH-HF) and hindcast maps (SWH-Hind) (the position of IWAV5 and HF radar are

438   respectively shown in **Figure 2**a and **2c**). The sea state information provided by the Mazara del

439   Vallo buoy was not taken into account in this analysis because of the long distance between

440   this instrument and the cyclone eye. We chose station IWAV5 because it is one of the nearest

441   stations to the cyclone eye. Also, as it is possible to see in **Figure 3a, b** and **c**, all the seismic

442   stations installed in the Sicily Channel area show very similar microseism amplitude patterns.

443   The time series of SWH-Hind was obtained by computing the median value of the SWH data

444   within a wide area of the Sicily Channel shown in **Figure 8d**. In general, the three datasets

445   exhibit a good agreement among them. In particular, we observe an increase that occurs almost

446   simultaneously for SWH-HF, SWH-Hind and the RMS amplitude. However, from the first

447   hours of 10 February, the SWH-HF started showing a different behavior compared to SWH-

448   Hind; indeed, the SWH-HF decreased while the SWH-Hind continued to show high values up

449   to the end of 10 February. This difference can be explained by considering that the HF Radar

450   provides information about the SWH for a limited area while SWH-Hind gives median

451   information about a wide area of the Sicily Channel. It is interesting to note that the microseism

452   amplitude follows more closely the areal sea state, shown by the SWH-Hind series, than the

453   punctual one, shown by the SWH-HF. We can note this in both a qualitative way in the time

454   series of **Figure 8a** and a quantitative way in the cross-plots of **Figures 8b** and **c**. For both the

455   cross-plots we calculated the R^2 value, to evaluate the goodness of the linear regression, and

456   we obtain R^2 values equal to 0.68 and 0.85, for the cross-plot RMS amplitude vs SWH-HF and

457   RMS amplitude vs SWH-Hind, respectively. The higher value of R^2 for the RMS amplitude -

458   SWH-Hind relationship can be explained by considering that microseism recorded by a seismic

459   station is generated by multiple extended sources distributed on a wide portion of the sea.

460   **4.4. Localization analysis**

461   As concerns the microseism source location, we performed the location analysis for the PM,

462   SM and SPSM using both the array techniques and the grid search method based on the seismic

463   amplitude decay. Concerning the array techniques, we chose to focus on the SM band since,

464   according to the information from the ARF, we expect reliable localizations only on the PM

465   and SM bands, while for the SPSM band appears spatial aliasing. As for the grid search method,

466   we obtained reliable locations only for the SM and SPSM bands, while for the PM band,

467   although we got localizations in agreement with the cyclone position, the associated R^2 values

468   turned out to be slightly lower than the threshold from which we can consider the locations

469   reliable.

470   By the grid search method, we obtained reliable locations from 9 February 2023 at 8:00 to 11

471   February 2023 at 00:00 (**Supplementary Figure 6**). In agreement with satellite images (**Figure**

472   **1**), on 9 February 2023, the sub-tropical system Helios was not yet well-developed and did not

473   show the cyclone eye. Indeed, during this day, we are able to locate a storm surge, probably

474   linked to the primitive formation of Helios, that occurred in the Ionian Sea. In particular, our

475   localizations, on 9 February from 8:00 to 20:00, indicate the source position near to the south-

476   eastern part of Sicily in agreement with the hindcast data showing for this area SWH greater

477   than 5 meters (**Figure 4b and 7**). During the following hours, our localizations

478   (**Supplementary Figure 6**) show a small but continuous shift of the source toward the Malta

479   area (**Figure 5**), in agreement with the relatively stable position of the cyclone eye for the first

480   hours of 10 February 2023, retrieved from SEVIRI data (**Figure 1**). Successively, the sub-

481   tropical system rapidly loses its strength and runs out completely on the day of 11 February

482   2023, making landfall against the Libyan coast. In **Table 1** we summarised the main features

483   of the microseism source located by using the grid search method during the days 9-10

484   February 2023 and compared these with the results obtained during the period 01:00 - 23:00 of

485   10 February 2023 in terms of the coordinates of the cyclone eye retrieved by SEVIRI data.

486   During the first hours of the cyclone life, the coordinates of the cyclone eye and the microseism

487   source show only a small offset that, as explained in section 3.4.1, can be due to the fact that

488   the point-like microseism source corresponds with the barycentric position of an extended

489   source and it is expected that the microseism source location could differ from the cyclone eye.

490   During the following hours, as shown in **Figure 1,** the cyclone moved southward until the time

491   when the cyclone made landfall against the Libyan coast. This shift is not visible in the

492   microseism location results, probably due to the lack of seismic stations in Africa, that would

493   help locate more accurately seismic sources placed close to the African Coastlines. In

494   **Supplementary Figure 7** we plot the temporal distribution of the R^2 values and compare this

495   with the SWH-Hind time series. These two datasets show a good agreement and highlight that

496   the higher R^2 values obtained from the grid search method are influenced by the presence of

497   the sub-tropical system Helios.

498   Concerning the array analysis, the result obtained for the PM band shows that, for the period

499   9-11 February, the back azimuth values pointed toward the Ionian Sea (**Supplementary Figure**

500   **8**) with apparent velocity values of ~ 3.0 km/s (**Supplementary Figure 9**). For the same days,

501   the back azimuth values for the SM band pointed toward the same region (**Supplementary**

502   **Figure 10**), with apparent velocity values of ~ 2.0 km/s (**Supplementary Figure 11**).

503   For the PM and the SPSM bands, we obtained reliable locations only by one of the two used

504   methods (array technique for the PM and grid search method for the SPSM), while for the SM

505   we obtained reliable locations from both the aforementioned methods and we can compare the

506   results obtained independently from these two methods. We can observe that the grid search

507   method based on the seismic amplitude decay is able to detect both the storm surge that

508   occurred in the Ionian sea and the following formation of the sub-tropical system Helios

509   (**Supplementary Figure 6**), and in particular by this method, we localize the cyclone as a

510   point-like source, considered as a barycentre of an extended source. The array technique

511   instead provides back azimuth values pointing toward the Ionian Sea for the entire period of 9-

512   11 February (**Supplementary Figure 10**). From these results, we can note that the two methods

513   are influenced by different sources. This different result can be explained based on the spatial

514   station distribution. Indeed, if we consider the grid search method we use a wide station

515   network including stations installed near the sub-tropical system Helios (MSDA, CLTA,

516   IWAV5, LINA and other stations), while the Etnean array includes 15 stations clustered in a

517   small area. In addition, the distance array center-Ionian Sea (~20 km) is smaller than the

518   distance array center-Sicily Channel (~90 km). During the period taken into account, we have

519   the coexistence of two strength sources, the first in the Ionian Sea (storm surge with SWH

520   greater than 5 m) and the other, probably the strongest, in the Sicily Channel (Helios), both

521   represented by the red contour line in **Figure 4c**. Hence, the coexistence of two sources and

522   the great difference in distance between the array center and the Ionian Sea and the array center

523   and the Sicily channel does not allow us to locate the sub-tropical system Helios with the array

524   technique, which gives us back azimuth values pointing always toward the nearest source.

525   **4.5. Seismic signature**

526   To show the main spectral characteristics of the sub-tropical system Helios, we used the method

527   developed by Soubestre et al. (2018). From our analysis, the evolution in time of the

528   microseism spectral characteristics between the first 24 hours and the following ones is evident

529   (**Figure 9**). In particular, with the vertical dashed lines in **Figure 9,** we show the time interval

530   when Helios develops, reaches the climax and loses power to run out. The first 24 hours are

531   characterized by the lack of a clear predominance of a particular frequency range. Starting from

532   early 9 February 2023 (first vertical white dashed line), we can observe high coherence values

533   clustered on a narrow frequency range between about 0.14 and 0.25 Hz, and this frequency

534   range is constant until the 80 hours (vertical black dashed line) corresponding to the morning

535   of 11 February. Successively, the frequency with the highest coherence starts to increase

536   reaching a value of about 0.35 Hz before the exhaustion of the phenomenon. This increase in

537   the frequency could be related to the landfall of Helios against the Lybian coast

538   (https://twitter.com/medcyclones/status/1624143740800536591?s=20, last access 23/05/2023

539   ). Indeed, as described in the literature (Gerstof et al., 2006; Lin et al., 2017; Sun et al., 2013),

540   there exists a relationship between the frequency, the sea depth and the development of local

541   wave motion near the coastline. In particular, Gerstof et al. (2006) show an increase in the

542   microseism frequency during the two landfalls of Hurricane Katrina. Similar results are shown

543   by Sun et al. (2013), who highlighted an increase in the intensity of the microseism for the SM

544   and SPSM and the frequency increase from the SM band toward the SPSM one during the

545   approaching of the three analyzed typhoons against the Chinese coast. Finally, Lin et al. (2017)

546   show an increase in the microseism frequency during the first landfall of typhoon Megi.

547   Similarly, we obtained an increase in frequency during the time interval when Helios

548   approached   the   Lybian   coastline   and   made   landfall   on   11   February

549   (https://twitter.com/medcyclones/status/1624143740800536591?s=20,   last   access

550   23/05/2023). We were also able to observe the gradual loss of power of the sub-tropical system

551   highlighted by ever-lower coherence values until its disappearance.

552   **5. Conclusions**

553   Several works have dealt with the relationship between microseism and several meteorological

554   phenomena, considering in particular storm surges (Ardhuin et al., 2019; Cannata et al., 2020;

555   Guerin et al., 2022; Moschella et al., 2020) and different types of cyclones (Borzì et al., 2022;

556   Bromirski, 2001; Bromirski et al., 2005; Gerstoft et al., 2006; Gualtieri et al., 2018; Lin et al.,

557   2017; Retailleau and Gualtieri, 2019, 2021; Zhang et al., 2010) that affect various parts of the

558   world (hurricanes, typhoons, tropical cyclones and medicanes). In this work, we analyzed the

559   relationship between the three main microseism bands (PM, SM and SPSM) and the sub-

560   tropical system Helios that occurred in the Mediterranean Sea during the time interval 9-11

561   February 2023. Although all the meteorological parameters suggest that Helios has not been

562   able to reach the fully Medicane characteristics, remaining a rather weak sub-tropical system,

563   the proximity of this cyclone to the southeastern Sicilian and Maltese coastal area has caused

564   heavy rainfall, strong wind gusts and violent storm surge in the two above mentioned areas.

565   To obtain information about the sea state we take into account the data of hindcast maps,

566   wavemeter buoy, HF radar and SEVIRI images. The first three methodologies show an increase

567   in the SWH during the period under investigation, with a climax during the days 9-10 February

568   2023, due to the presence of the sub-tropical system Helios. In particular, the HF radar and the

569   hindcast maps exhibit an SWH of about 6 meters while the wavemeter buoy shows an SWH of

570   about 3 meters. This difference is only linked to the position where the two instruments are

571   installed, indeed the HF radar is installed at about 90 km from the cyclone eye while the

572   wavemeter buoy is installed at about 190 km. SEVIRI images provide information about the

573   location of the cyclone eye that is clearly visible between 01:00 and 23:00 on 10 February

574   2023.

575   To analyze this meteorological phenomenon from a seismic point of view, we selected 120

576   seismic stations installed along the Italian, Maltese and Greek coastal areas: i) 105 used in

577   spectral and amplitude analysis, in the grid search method and 4 of these to obtain the seismic

578   signature of Helios using the method of the covariance matrix; ii) 15 in array analysis. The

579   results, obtained from the spectral analysis, highlight that the seismic signals, in particular the

580   PM, SM and SPSM bands, are affected by the storm surge and by the sub-tropical system

581   Helios. This is evident considering the RMS amplitude time series, the spectrograms and the

582   RMS amplitude space-time distribution, in which it is possible to observe that the amplitude of

583   the microseism signal, in the three main bands above mentioned, shows a similar trend and it

584   is greater during the period 9-10 February 2023 for the stations installed close to the Sicily

585   Channel (for example the stations MSDA, LINA and IWAV5), while the stations installed

586   farther from Helios (for example CELB) show a different behavior conditioned by local

587   sources. Furthermore, the increase of the RMS amplitude for the PM band can be explained on

588   the basis of the position where Helios develops. Indeed, as explained in the literature

589   (Bromirski et al., 2005), the generation of the PM is limited in the areas where the depth of the

590   sea bottom is smaller than ½λ (where λ is the wavelength of the sea waves) as a consequence

591   of the amplitude decay of the pressure fluctuations. The Sicily Channel and in particular the

592   area between Malta and Sicily (Malta Channel), where Helios stood still for the entire 10

593   February 2023, shows an average depth of about 65 m b.s.l., and considering wavelength

594   between ∼45 m and ∼150 m it is possible the generation of the PM for this area.

595   By comparing the SWH recorded by HF Radar, SWH retrieved by hindcast data and the RMS

596   amplitude recorded at the station IWAV5, we observe that the RMS amplitude time series

597   shows a trend more similar to that of hindcast data than to the HF Radar data. This could be

598   explained by considering that the microseism is a seismic signal generated by multiple and

599   extended sources in a large area of the sea and hence its amplitude is related to the state of a

600   wide portion of the sea.

601   We used two different methods to track the position of the sub-tropical system Helios during

602   its lifetime and, through the performed analysis, we were able to locate both the storm surge

603   that occurred in the Ionian Sea and Helios. In particular, using the grid search method based on

604   the seismic amplitude decay we located the storm surge in the Ionian Sea on 9 February 2023

605   and the sub-tropical system Helios on the next day, while with the array technique, we located

606   only the storm surge in the Ionian Sea as a consequence of the position of the array closer to

607   the Ionian Sea than to the Sicily Channel. The location obtained both for the storm surge and

608   for the sub-tropical system Helios, during the first hours of its life, is in agreement with the real

609   position of the two meteorological phenomena shown by the hindcast maps and satellite

610   images. Successively, the sub-topical system Helios moved southward until the time when the

611   cyclone made landfall against the Libyan coast while the microseism source continued to show

612   a stable position near Malta Island. This difference between the two positions is probably due

613   to the lack of seismic stations in Africa, that does not locate accurately microseism sources

614   placed close to the African Coastlines. In addition, using the method of the covariance matrix,

615   we obtained the seismic signature of the sub-tropical system Helios. In particular, during the

616   development and climax of the cyclone Helios, we can observe high coherence values clustered

617   on a narrow frequency range between about 0.14 and 0.25 Hz that, as described in the literature,

618   corresponds to the microseism bands (SM and SPSM) most affected by cyclonic activity. This

619   narrow frequency range stays constant until the time when Helios makes landfall when we

620   observe an increase in the frequency until a value of about 0.35 Hz probably linked to the

621   decrease of the sea depth and the development of local wave motion near the coastline.

622   Starting from Borzì et al. (2022), this work aims at studying and monitoring the Mediterranean

623   cyclones through microseism and its integration with sea state data. It underlines that it is

624   possible to extract information about these meteorological phenomena by an innovative system

625   for the sea state monitoring that includes not only the classical instruments (such as wavemeter

626   buoys, radar HF and geostationary satellites) but also seismometers. In particular, the large

627   number of broadband seismic stations, installed for earthquake and volcanic monitoring, can

628   compensate for the lack of data of the classical instruments mentioned above, more often

629   affected by instrument breakage.

630   Finally, since we obtained the seismic signature of this particular Mediterranean cyclone we

631   can compare it with the seismic signature of other Mediterranean events (Medicane and

632   common storms) to identify the similarities and differences in the spectral content of different

633   Mediterranean cyclones and other more common events. The characterization of the seismic

634   signature of these events could be useful to identify Mediterranean cyclones by old

635   seismograms, and hence to reconstruct the temporal variability (in terms of occurrence rate and

636   intensity) of these extreme meteo-marine events whose evolution seems to be strictly linked to

637   the global warming (e.g. Emanuel, 2005; Reguero et al., 2019).

638

639

Data availability

The seismic data, in the miniseed format used in this study, can be downloaded through the

ORFEUS-EIDA database (http://www.orfeus-eu.org/data/eida/). All the seismic stations used

in this study, along with their main features, are reported in Supplementary Tables 1 and 2. The

hindcast data are available online on the Copernicus site

(https://resources.marine.copernicus.eu/products). The Italian buoy data (Mazara del Vallo) are

available on the ISPRA website (https://dati.isprambiente.it/) and on the MAREOGRAFICO

website (www.mareografico.it). Satellite data are available on the EUMETSAT website

(https://navigator.eumetsat.int/product/EO:EUM:DAT:MSG:HRSEVIRI). The HF Radar data

are available on the CALYPSO project website by compiling the form indicated on the web

page (https://www.calypsosouth.eu/index.php/welcome/open_page/50/0) or by contacting

giuseppe.ciraolo@unipa.it or salvatore.aronica@cnr.it.

Acknowledgments

The authors thank the i-waveNET "Implementation of an innovative system for monitoring the

state of the sea in climate change scenarios" project, funded by the Interreg Italia-Malta

Programme (https://iwavenet.eu/; notice 2/2019 Axis 3; project code C2-3.2-106). A.M.B.

thanks the PON "Ricerca e Innovazione 2014-2020 Azione IV.5 - Dottorati su tematiche

green". The authors are grateful to Prof. Vittorio Scribano, the Museo Archeologico di

Kamarina, Parco di Kamarina e Cava D'Ispica - Direttore Arch. Domenico Buzzone and the

Centro Polifunzionale di Protezione Civile - Dott.ssa Emilia Pluchinotta, for hosting the

seismic stations installed in the framework of the i-waveNET project and used in this work

(IWAV2, IWAV3, IWAV3). This study has been conducted using E.U. Copernicus Marine

Service Information, https://doi.org/10.25423/cmcc/medsea_multiyear_wav_006_012. The

seismic data, downloaded using the EIDA and ORFEUS webservices, belong to the AC, FR,

664 HC, HL, HP, IV, ML and MN networks. T.L. and R.D.P. thank the research project

665 "SEISMOSTORM" funded by the BRAIN-be 2 program of the Federal Science Policy

666 (BELSPO).

667

668

669 **References**

670

671 ● Agenzia per la Protezione dell'Ambiente e per i Servizi Tecnici Dipartimento Tutela

672 Acque Interne e Marine Servizio Mareografico - Atlante delle onde nei mari italiani -

673 Università   degli   studi   di   Roma   Tre

674 http://opac.apat.it/sebina/repository/catalogazione/immagini/pdf/atlante%20mari%201

675 _60_2_.pdf

676 ● Androulidakis, Y., Makris, C., Mallios, Z., Pytharoulis, I., Baltikas, V., & Krestenitis,

677 Y. Storm surges during a Medicane in the Ionian Sea. *Proceedings of the Marine and*

678 *Inland Waters Research Symposium, Porto Heli, Greece*. p. 16-19, 2022..

679 ● Ardhuin, F., & Roland, A. "Coastal wave reflection, directional spread, and

680 seismoacoustic noise sources." *Journal of Geophysical Research: Oceans* 117.C11,

681 2012.

682 ● Ardhuin, F.; Gualtieri, L.; Stutzmann, E. How ocean waves rock the Earth: Two

683 mechanisms explain microseisms with periods 3 to 300 s. *Geophysical Research*

684 *Letters*, 42.3: 765-772, https://doi.org/10.1002/2014GL062782, 2015.

685 ● Ardhuin, F., Stopa, J. E., Chapron, B., Collard, F., Husson, R., Jensen, R. E., ... &

686 Young, I. Observing sea states. *Frontiers in Marine Science*, 124,

687 https://doi.org/10.3389/fmars.2019.00124, 2019.

688   ● Battaglia, J., & Aki, K. Location of seismic events and eruptive fissures on the Piton de

689   la Fournaise volcano using seismic amplitudes. *Journal of Geophysical Research: Solid*

690   *Earth*, *108*(B8), https://doi.org/10.1029/2002JB002193, 2003.

691   ● Battaglia, J., Aki, K., & Ferrazzini, V. Location of tremor sources and estimation of

692   lava output using tremor source amplitude on the Piton de la Fournaise volcano: 1.

693   Location of tremor sources. Journal of volcanology and geothermal research, 147(3-4),

694   268-290, https://doi.org/10.1016/j.jvolgeores.2005.04.005, 2005.

695   ● Bencivenga, M., Nardone, G., Ruggiero, F., & Calore, D., The Italian Data Buoy

696   Network. *WTI Trans. Eng. Sci.*, 74, 321–332, 2012.

697   ● Borzì, A. M., Minio, V., Cannavò, F., Cavallaro, A., D'Amico, S., Gauci, A., ... &

698   Cannata, A. Monitoring extreme meteo-marine events in the Mediterranean area using

699   the microseism (Medicane Apollo case study). *Scientific Reports*, *12*(1), 21363,

700   https://doi.org/10.1038/s41598-022-25395-9, 2022.

701   ● Bouin, M. N., & Lebeaupin Brossier, C. Surface processes in the 7 November 2014

702   medicane from air–sea coupled high-resolution numerical modelling. *Atmospheric*

703   *Chemistry and Physics*, *20*(11), 6861-6881, 2020.

704   ● Bromirski, Peter D., Reinhard E. Flick, and Nicholas Graham. "Ocean wave height

705   determined from inland seismometer data: Implications for investigating wave climate

706   changes in the NE Pacific." *Journal of Geophysical Research: Oceans* 104.C9 20753-

707   20766, https://doi.org/10.1029/1999JC900156, 1999.

708   ● Bromirski, Peter D. "Vibrations from the "perfect storm"." *Geochemistry, Geophysics,*

709   *Geosystems* 2.7, https://doi.org/10.1029/2000GC000119, 2001.

710   ● Bromirski, Peter D., Fred K. Duennebier, and Ralph A. Stephen. "Mid-ocean

711   microseisms." *Geochemistry,   Geophysics,   Geosystems*   6.4,

712   https://doi.org/10.1029/2004GC000768, 2005.

713 ● Cannata, A., Di Grazia, G., Aliotta, M., Cassisi, C., Montalto, P., & Patanè, D.

714 Monitoring seismo-volcanic and infrasonic signals at volcanoes: Mt. Etna case study.

715 *Pure and Applied Geophysics*, *170*, 1751-1771, https://doi.org/10.1007/s00024-012-

716 0634-x, 2013.

717 ● Cannata, A., Cannavò, F., Moschella, S., Di Grazia, G., Nardone, G., Orasi, A., ... &

718 Gresta, S. Unravelling the relationship between microseisms and spatial distribution of

719 sea wave height by statistical and machine learning approaches. *Remote Sensing*, *12*(5),

720 761, https://doi.org/10.3390/rs12050761, 2020.

721 ● Carrió, D. S., Homar, V., Jansa, A., Romero, R., & Picornell, M. A. Tropicalization

722 process of the 7 November 2014 Mediterranean cyclone: Numerical sensitivity study.

723 *Atmospheric Research*, *197*, 300-312, https://doi.org/10.1016/j.atmosres.2017.07.018,

724 2017.

725 ● Capodici, F., Cosoli, S., Ciraolo, G., Nasello, C., Maltese, A., Poulain, P. M., ... &

726 Gauci, A. Validation of HF radar sea surface currents in the Malta-Sicily Channel.

727 *Remote sensing of environment*, *225*, 65-76, https://doi.org/10.1016/j.rse.2019.02.026,

728 2019.

729 ● Cavicchia, Leone, Hans von Storch, and Silvio Gualdi. "Mediterranean tropical-like

730 cyclones in present and future climate." *Journal of Climate* 27.19, 7493-7501,

731 https://doi.org/10.1175/JCLI-D-14-00339.1, 2014.

732 ● Comellas Prat, A., Federico, S., Torcasio, R. C., D'Adderio, L. P., Dietrich, S., &

733 Panegrossi, G. Evaluation of the sensitivity of medicane Ianos to model microphysics

734 and initial conditions using satellite measurements. *Remote Sensing*, *13*(24), 4984,

735 https://doi.org/10.3390/rs13244984, 2021.

736 ● Cutroneo, L., Ferretti, G., Barani, S., Scafidi, D., De Leo, F., Besio, G., & Capello, M..

737 Near real-time monitoring of significant sea wave height through microseism

738   recordings: Analysis of an exceptional sea storm event. *Journal of Marine Science and*

739   *Engineering*, *9*(3), 319, https://doi.org/10.3390/jmse9030319, 2021.

740   ● Dafis, S., Rysman, J. F., Claud, C., & Flaounas, E. Remote sensing of deep convection

741   within a tropical-like cyclone over the Mediterranean Sea. *Atmospheric Science Letters*,

742   *19*(6), e823, https://doi.org/10.1002/asl.823, 2018.

743   ● Davies R. Cyclone Helios, Malta and Italy, February 2023,

744   https://www.efas.eu/en/news/cyclone-helios-malta-and-italy-february-2023, last

745   access 13/04/2023)

746   ● Delibera di Giunta - Regione Siciliana

747   (https://www2.regione.sicilia.it/deliberegiunta/file/giunta/allegati/N.099_15.02.2023.p

748   df, last access 13/04/2023)

749   ● Di Muzio, E., Riemer, M., Fink, A. H., & Maier-Gerber, M. Assessing the predictability

750   of Medicanes in ECMWF ensemble forecasts using an object-based approach.

751   *Quarterly Journal of the Royal Meteorological Society*, *145*(720), 1202-1217,

752   https://doi.org/10.1002/qj.3489, 2019.

753   ● Emanuel, K. Increasing destructiveness of tropical cyclones over the past 30 years.

754   *Nature*, *436*(7051), 686-688, https://doi.org/10.1038/nature03906, 2005.

755   ● Faranda, D., Bourdin, S., Ginesta, M., Krouma, M., Noyelle, R., Pons, F., ... & Messori,

756   G. A climate-change attribution retrospective of some impactful weather extremes of

757   2021. *Weather and Climate Dynamics*, *3*(4), 1311-1340, https://doi.org/10.5194/wcd-

758   3-1311-2022, 2022.

759   ● Ferretti, G., Zunino, A., Scafidi, D., Barani, S., & Spallarossa, D. On microseisms

760   recorded near the Ligurian coast (Italy) and their relationship with sea wave height.

761   *Geophysical Journal International*, *194*(1), 524-533,

762   https://doi.org/10.1093/gji/ggt114, 2013.

763   ● Ferretti, G., Barani, S., Scafidi, D., Capello, M., Cutroneo, L., Vagge, G., & Besio, G.

764   Near real-time monitoring of significant sea wave height through microseism

765   recordings: An application in the Ligurian Sea (Italy). *Ocean & Coastal Management*,

766   *165*, 185-194, https://doi.org/10.3390/jmse9030319, 2018.

767   ● Flaounas, E., Davolio, S., Raveh-Rubin, S., Pantillon, F., Miglietta, M. M., Gaertner,

768   M. A., ... & Ricard, D. Mediterranean cyclones: Current knowledge and open questions

769   on dynamics, prediction, climatology and impacts. *Weather and Climate Dynamics*,

770   *3*(1), 173-208, https://doi.org/10.5194/wcd-3-173-2022, 2022.

771   ● Gerstoft, P., Fehler, M. C., & Sabra, K. G. When katrina hit california. *Geophysical*

772   *Research Letters*, *33*(17), https://doi.org/10.1029/2006GL027270, 2006.

773   ● Gualtieri, L., Camargo, S. J., Pascale, S., Pons, F. M., & Ekström, G. The persistent

774   signature of tropical cyclones in ambient seismic noise. *Earth and Planetary Science*

775   *Letters*, *484*, 287-294, https://doi.org/10.1016/j.epsl.2017.12.026, 2018.

776   ● Guerin, G., Rivet, D., Van Den Ende, M. P. A., Stutzmann, E., Sladen, A., & Ampuero,

777   J. P. Quantifying microseismic noise generation from coastal reflection of gravity

778   waves recorded by seafloor DAS. *Geophysical Journal International*, *231*(1), 394-407,

779   https://doi.org/10.1093/gji/ggac200, 2022.

780   ● Hart, R. E. A cyclone phase space derived from thermal wind and thermal asymmetry.

781   *Monthly weather review*, *131*(4), 585-616, https://doi.org/10.1175/1520-

782   0493(2003)131%3C0585:ACPSDF%3E2.0.CO;2, 2003.

783   ● Hasselmann, Klaus. "A statistical analysis of the generation of microseisms." *Reviews*

784   *of Geophysics* 1.2, 177-210, 1963.

785   ● Haubrich, Richard A., and Keith McCamy. "Microseisms: Coastal and pelagic

786   sources." *Reviews of Geophysics* 7.3: 539-571, 1969.

787 ● Kerkmann J. and Bachmeier S. Development of a tropical storm in the Mediterranean

788   Sea (6–9 November 2011). Available at: https://www.eumetsat.int/tropical-storm-

789   develops-mediterranean-sea (last access: 15 February 2023), 2011.

790 ● Korres, G., Ravdas, M., & Zacharioudaki, A. Mediterranean Sea Waves Hindcast

791   (CMEMS MED-Waves) [Data set]. Copernicus Monitoring Environment Marine

792   Service   (CMEMS).

793   https://doi.org/10.25423/CMCC/MEDSEA_HINDCAST_WAV_006_012, 2019

794 ● Kumagai, H., Placios, P., Ruiz, M., Yepes, H., & Kozono, T. Ascending seismic source

795   during an explosive eruption at Tungurahua volcano, Ecuador. *Geophysical Research*

796   *Letters*, *38*(1), https://doi.org/10.1029/2010GL045944, 2011.

797 ● Lagouvardos, K., Karagiannidis, A., Dafis, S., Kalimeris, A., & Kotroni, V. Ianos—A

798   hurricane in the Mediterranean. *Bulletin of the American Meteorological Society*,

799   *103*(6), E1621-E1636, https://doi.org/10.1175/BAMS-D-20-0274.1, 2022.

800 ● Lin, J., Lin, J., & Xu, M. Microseisms generated by super typhoon Megi in the western

801   Pacific Ocean. *Journal of Geophysical Research: Oceans*, *122*(12), 9518-9529,

802   https://doi.org/10.1002/2017JC013310, 2017.

803 ● Lionello, P., Conte, D., & Reale, M. The effect of cyclones crossing the Mediterranean

804   region on sea level anomalies on the Mediterranean Sea coast. *Natural Hazards and*

805   *Earth System Sciences*, *19*(7), 1541-1564, https://doi.org/10.5194/nhess-19-1541-2019,

806   2019.

807 ● Long, R. M., Barrick, D., Largier, J. L., & Garfield, N. Wave observations from central

808   California: SeaSonde systems and in situ wave buoys. *Journal of Sensors*,

809   https://doi.org/10.1155/2011/728936, *2011*.

810 ● Longuet-Higgins, Michael Selwyn. "A theory of the origin of microseisms."

811 *Philosophical Transactions of the Royal Society of London. Series A, Mathematical and*

812 *Physical Sciences* 243.857, 1-35, 1950.

813 ● Lorente, P., Lin-Ye, J., Garcia-Leon, M., Reyes, E., Fernandes, M., Sotillo, M. G., ...

814 & Alvarez-Fanjul, E. On the performance of high frequency radar in the western

815 mediterranean during the record-breaking storm gloria. *Frontiers in Marine Science*, *8*,

816 645762, https://doi.org/10.3389/fmars.2021.645762, 2021.

817 ● Miglietta, M. M., Moscatello, A., Conte, D., Mannarini, G., Lacorata, G., & Rotunno,

818 R. Numerical analysis of a Mediterranean 'hurricane' over south-eastern Italy:

819 Sensitivity experiments to sea surface temperature. *Atmospheric research*, *101*(1-2),

820 412-426, https://doi.org/10.1016/j.atmosres.2011.04.006, 2011.

821 ● Miglietta, M. M., Laviola, S., Malvaldi, A., Conte, D., Levizzani, V., & Price, C.

822 Analysis of tropical-like cyclones over the Mediterranean Sea through a combined

823 modeling and satellite approach. *Geophysical Research Letters*, *40*(10), 2400-2405,

824 https://doi.org/10.1002/grl.50432, 2013.

825 ● Miglietta, M. M., & Rotunno, R. Development mechanisms for Mediterranean tropical-

826 like cyclones (medicanes). *Quarterly Journal of the Royal Meteorological Society*,

827 *145*(721), 1444-1460, https://doi.org/10.1002/qj.3503, 2019.

828 ● Moschella, S., Cannata, A., Cannavò, F., Di Grazia, G., Nardone, G., Orasi, A., ... &

829 Gresta, S. Insights into microseism sources by array and machine learning techniques:

830 Ionian and Tyrrhenian sea case of study. *Frontiers in Earth Science*, *8*, 114,

831 https://doi.org/10.3389/feart.2020.00114, 2020.

832 ● Nastos, P. T., Papadimou, K. K., & Matsangouras, I. T. Mediterranean tropical-like

833 cyclones: Impacts and composite daily means and anomalies of synoptic patterns.

834   *Atmospheric Research*, *208*, 156-166, https://doi.org/10.1016/j.atmosres.2017.10.023,

835   2018.

836   ●   Oliver, J., & Page, R. Concurrent storms of long and ultralong period microseisms.

837   *Bulletin of the Seismological Society of America*, *53*(1), 15-26, 1963.

838   ●   Orasi, A., Picone, M., Drago, A., Capodici, F., Gauci, A., Nardone, G., ... & Alonso-

839   Martirena, A. HF radar for wind waves measurements in the Malta-Sicily Channel.

840   *Measurement*, *128*, 446-454, https://doi.org/10.1016/j.measurement.2018.06.060,

841   2018.

842   ●   Pravia-Sarabia, E., Gómez-Navarro, J. J., Jiménez-Guerrero, P., & Montávez, J. P.

843   Influence of sea salt aerosols on the development of Mediterranean tropical-like

844   cyclones. *Atmospheric   Chemistry   and   Physics*, *21*(17),   13353-13368,

845   https://doi.org/10.5194/acp-21-13353-2021, 2021.

846   ●   Portmann, R., González-Alemán, J. J., Sprenger, M., & Wernli, H. How an uncertain

847   short-wave perturbation on the North Atlantic wave guide affects the forecast of an

848   intense Mediterranean cyclone (Medicane Zorbas). *Weather and Climate Dynamics*,

849   *1*(2), 597-615, https://doi.org/10.5194/wcd-1-597-2020, 2020.

850   ●   Reguero, B. G., Losada, I. J., & Méndez, F. J. A recent increase in global wave power

851   as a consequence of oceanic warming. *Nature communications*, *10*(1), 205,

852   https://doi.org/10.1038/s41467-018-08066-0, 2019.

853   ●   Retailleau, L., & Gualtieri, L. Toward high-resolution period-dependent seismic

854   monitoring of tropical cyclones. *Geophysical Research Letters*, *46*(3), 1329-1337,

855   https://doi.org/10.1029/2018GL080785, 2019.

856   ●   Retailleau, L., & Gualtieri, L. Multi-phase seismic source imprint of tropical cyclones.

857   *Nature communications*, *12*(1), 2064, https://doi.org/10.1038/s41467-021-22231-y,

858   2021.

859   ● Rost, S., & Thomas, C. Array seismology: Methods and applications. *Reviews of*

860   *geophysics*, *40*(3), 2-1, https://doi.org/10.1029/2000RG000100, 2002.

861   ● Rumora, I., Jukić, O., Filić, M., & Filjar, R. A study of GPS positioning error associated

862   with tropospheric delay during Numa Mediterranean cyclone. *Int J for Transp and Traff*

863   *Eng*, *8*(3), 282-293, https://doi.org/10.7708/ijtte.2018.8(3).03, 2018.

864   ● Sarpkaya, T., & Isaacson, M. Mechanics of wave forces on offshore structures Van

865   Nostrand Reinhold Company New York. *New York,* 1981.

866   ● Saviano, S., Kalampokis, A., Zambianchi, E., & Uttieri, M. A year-long assessment of

867   wave measurements retrieved from an HF radar network in the Gulf of Naples

868   (Tyrrhenian Sea, Western Mediterranean Sea). *Journal of Operational Oceanography*,

869   *12*(1), 1-15, https://doi.org/10.1080/1755876X.2019.1565853, 2019.

870   ● Scardino, G., Scicchitano, G., Chirivì M., Costa P.J.M., Luparelli A., Mastronuzzi G.

871   Convolutional Neural Network and Optical Flow for the Assessment ofWave and Tide

872   Parameters from Video Analysis (LEUCOTEA): An Innovative Tool for Coastal

873   Monitoring. Remote Sensing, 14, 2994, doi.org/10.3390/rs14132994, 2022.

874   ● Scicchitano, G., Scardino, G., Monaco, C., Piscitelli, A., Milella, M., De Giosa, F., &

875   Mastronuzzi, G. Comparing impact effects of common storms and Medicanes along the

876   coast of south-eastern Sicily. *Marine Geology*, *439*, 106556,

877   https://doi.org/10.1016/j.margeo.2021.106556, 2021.

878   ● Shaltout, M., & Omstedt, A. Recent sea surface temperature trends and future scenarios

879   for the Mediterranean Sea. *Oceanologia*, *56*(3), 411-443, https://doi.org/10.5697/oc.56-

880   3.411, 2014.

881   ● Soubestre, J., Shapiro, N. M., Seydoux, L., de Rosny, J., Droznin, D. V., Droznina, S.

882   Y., ... & Gordeev, E. I. Network-based detection and classification of seismovolcanic

883   tremors: Example from the Klyuchevskoy volcanic group in Kamchatka. *Journal of*

884   *Geophysical Research: Solid Earth*, *123*(1), 564-582,

885   https://doi.org/10.1002/2017JB014726, 2018.

886   ● Sun, T., Xue, M., Le, K. P., Zhang, Y., & Xu, H. Signatures of ocean storms on seismic

887   records in South China Sea and East China Sea. *Marine Geophysical Research*, *34*,

888   431-448, https://doi.org/10.1007/s11001-013-9204-6, 2013.

889   ● Tous, M., & Romero, R. Meteorological environments associated with medicane

890   development. *International Journal of Climatology*, *33*(1), 1-14,

891   https://doi.org/10.1002/joc.3428, 2013.

892   ● Trnkoczy, A., Bormann, P., Hanka, W., Holcomb, L. G., Nigbor, R. L., Shinohara, M.,

893   ... & Suyehiro, K. Site selection, preparation and installation of seismic stations. In *New*

894   *Manual of Seismological Observatory Practice 2 (NMSOP-2)* (pp. 1-139). Deutsches

895   GeoForschungsZentrum GFZ, 2012.

896   ● Tweet   medcyclones:

897   https://twitter.com/medcyclones/status/1623795373423620096?s=20,

898   https://twitter.com/medcyclones/status/1623992335104081921?s=20,

899   ● https://twitter.com/medcyclones/status/1624143740800536591?s=20

900   ● Varlas, G., Vervatis, V., Spyrou, C., Papadopoulou, E., Papadopoulos, A., &

901   Katsafados, P. Investigating the impact of atmosphere–wave–ocean interactions on a

902   Mediterranean tropical-like cyclone. *Ocean Modelling*, *153*, 101675,

903   https://doi.org/10.1016/j.ocemod.2020.101675, 2020.

904   ● Welch, P. D. The use of Fast Fourier Transform for the estimation of power spectra: a

905   method based on time averaging over short, modified periodograms, IEEE T. Audio

906   Electroacoust. 15, 70–73, https://doi.org/10.1109/TAU.1967.1161901, 1967.

907   •   Zhang, J., Gerstoft, P., & Bromirski, P. D. Pelagic and coastal sources of P-wave

908   microseisms: Generation under tropical cyclones. *Geophysical Research Letters*,

909   *37*(15), https://doi.org/10.1029/2010GL044288, 2010.

910   •   Zimbo, F., Ingemi, D., & Guidi, G. The tropical-like cyclone "ianos" in September

911   2020. *Meteorology*, *1*(1), 29-44, https://doi.org/10.3390/meteorology1010004, 2022.

912

913

914

915

916

Authors Contribution

918 A.M.B., A.C. and F.C. conceived the idea. A.M.B. analyzed seismic data and V.M. performed

919 array analysis. C.L.R, G.N., A.O. and M.P. analyzed buoys data. S.A., D.C., G.D.G., G.L.,

920 S.D., R.D. and T.L. helped perform seismic analysis. F.C., G.C., S.A., I.F., G.G. G.M.,

921 analyzed HF Radar Data. A.M.B. and V.M. wrote the paper. S.A., F.C., D.C., G.L. and V.M.

922 dealt with the new seismic installation. G.C. lead one of the projects funding this research, G.S.

923 helped to interpret the sea state data. All the authors discussed the results, edited the paper and

924 gave consent for this publication under the supervision of A.C.

925

926

927

928

929

930

931
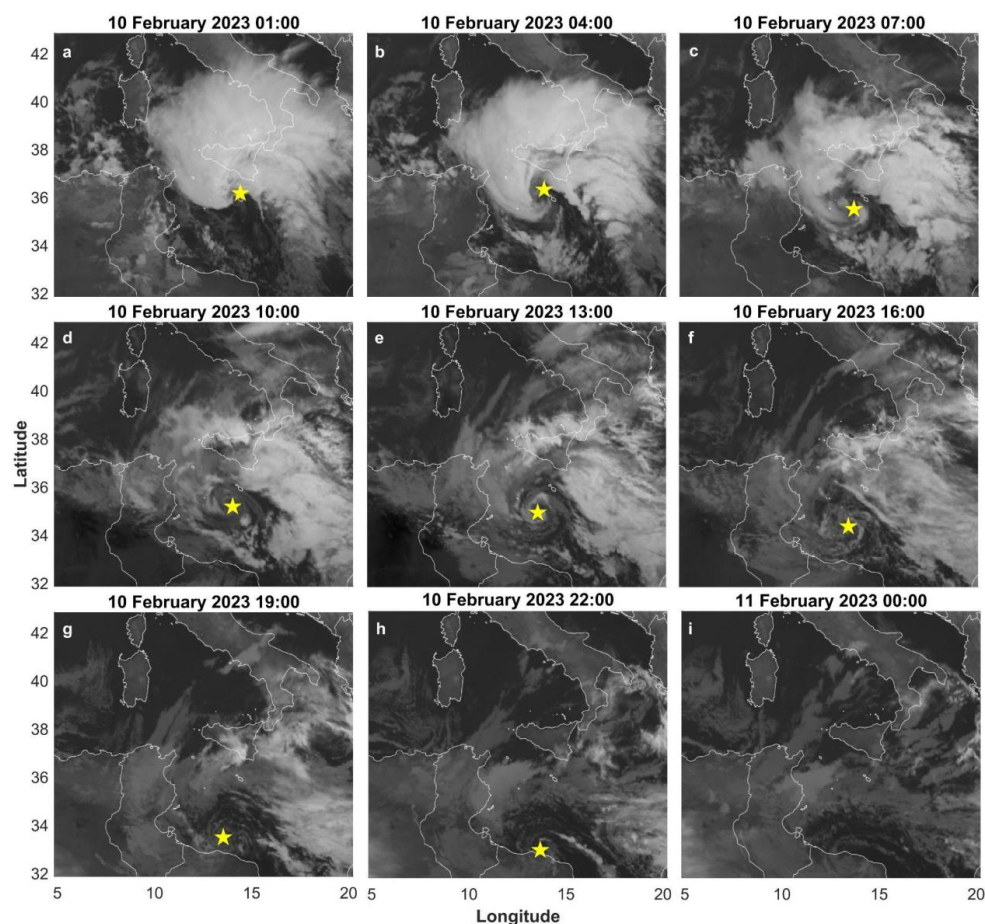
Figures

Figure 1: Satellite images of the Mediterranean area and of the sub-tropical system Helios during the period 10/02/2023 01:00 - 11/02/2023 00:00. The yellow stars in (a-h) show the position of the cyclone eye. The lack of the star in (i) is due to the dissipation of Helios after the landfall against the Libyan coast (h). (©EUMETSAT SEVIRI Images)
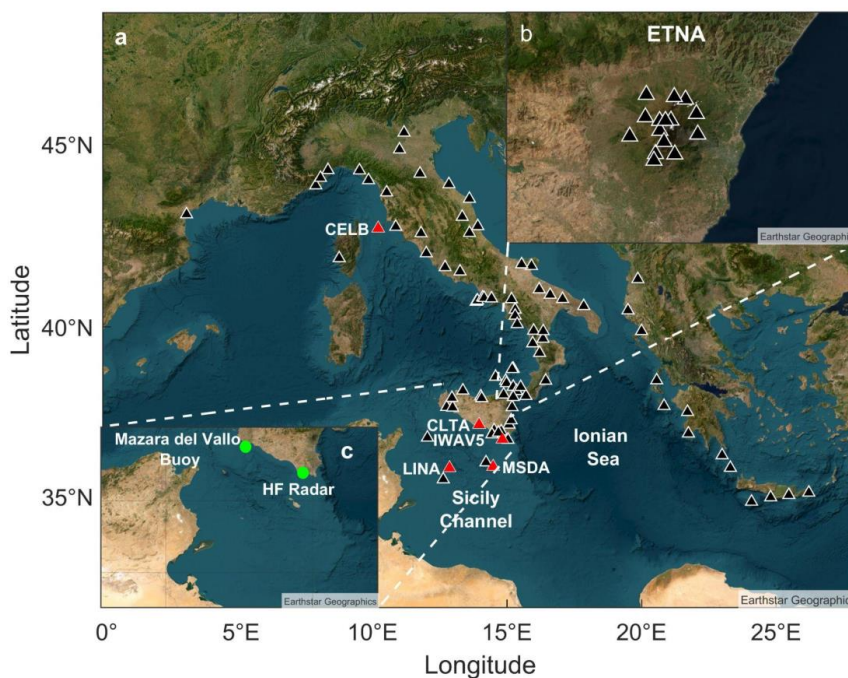
938

939 **Figure 2:** Satellite image of the Mediterranean area with a selection of the broadband seismic

940 stations available in the ORFEUS and INGV databases and used in the spectral analysis and in

941 the grid search method (a) and selection of the broadband seismic stations in the Etna area

942 maintained by INGV-OE (b), used in the array analysis (base image source ©Earthstar

943 Geographic). The red triangles indicate the stations used in the detailed analysis shown in

944 Figures **3** and **9** and in **Supplementary Figures 1** and **2**. The green dots in (c) indicate the

945 position of the wavemeter buoy (Mazara del Vallo) and of the HF Radar (Marina di Ragusa)

946 used for the sea state monitoring.
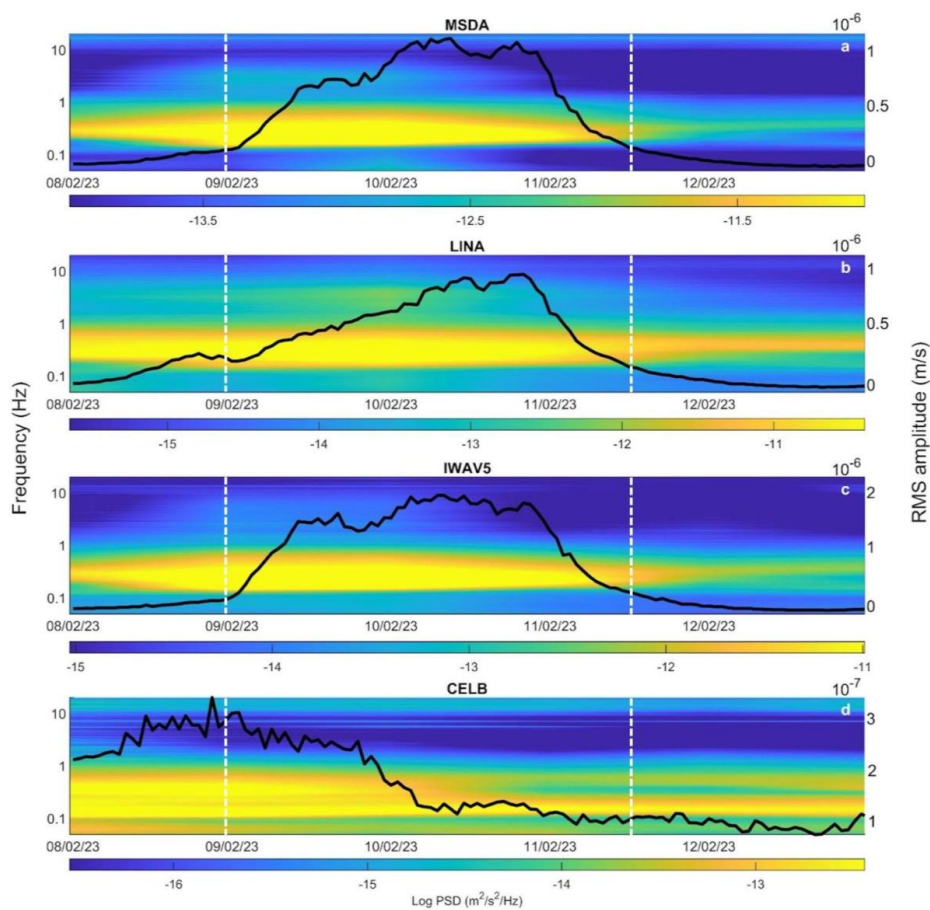
Figure 3: Spectrograms and RMS amplitude time series for the SM band (0.1-0.2 Hz) of the seismic signal recorded by the vertical component of 4 stations located along the Maltese coastline (a), in Linosa Island (b), in the southern part of Sicily (c) and in Central Italy (d) (see **Figure 2a** for the station locations).

2000
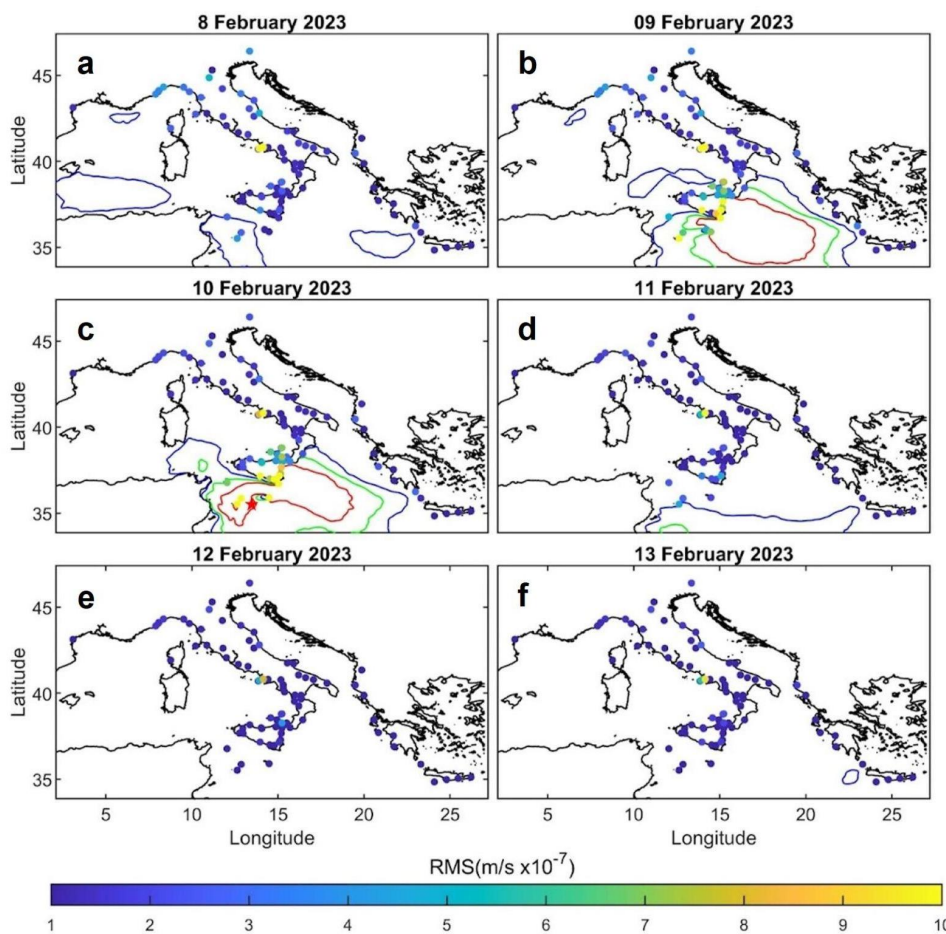
Figure 4: Spatial and temporal distribution of the RMS amplitude for the SM band computed at the 105 stations considered (dots). The colors of dots represent the RMS amplitude as specified in the color bar. The blue, green and red contour lines represent significant wave heights of 3, 4 and 5 m, respectively, while the red five-point star in (c) indicates the eye position of the sub-tropical system Helios obtained from satellite images.
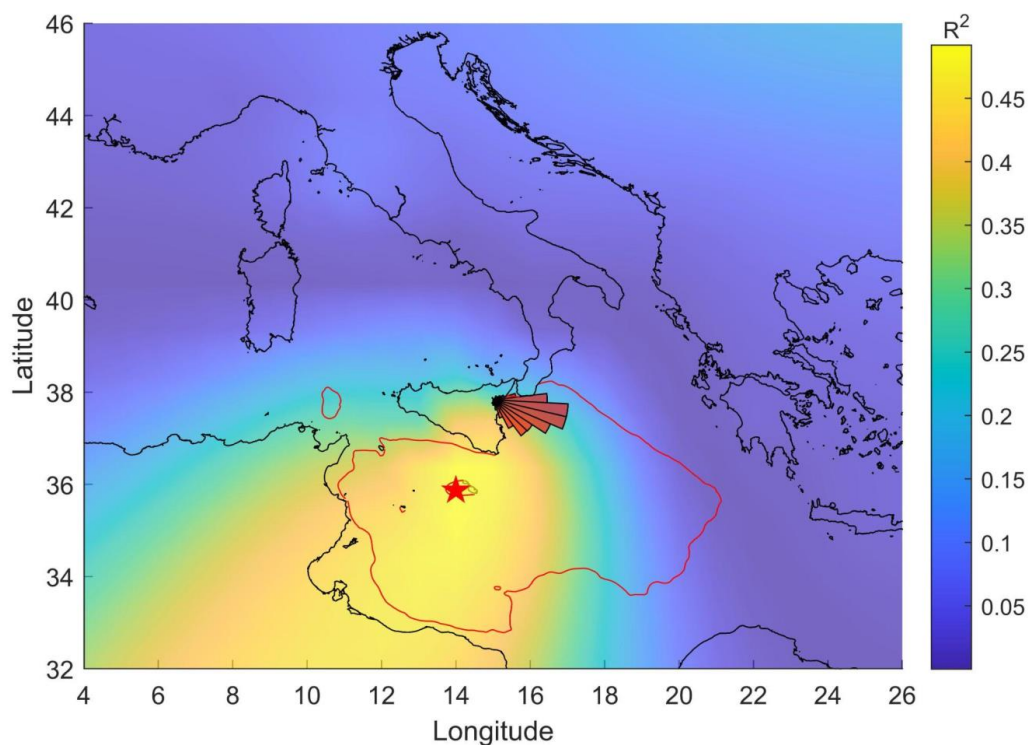
Figure 5: Localization of the microseism source for 10 February 2023 at 16:00. The red five-point star indicates the centroid position of all the grid nodes whose R^2 values do not differ by more than 1% from the maximum R^2 value obtained with the grid search method, while the rose diagram, located at the center of the summit area of Mt. Etna (see **Figure 2b**), shows the distribution of the back azimuth values on the same day. The red contour line represents significant wave heights of 4 m obtained from the Copernicus product MEDSEA_HINDCAST_WAV_006_012 during the same time interval.
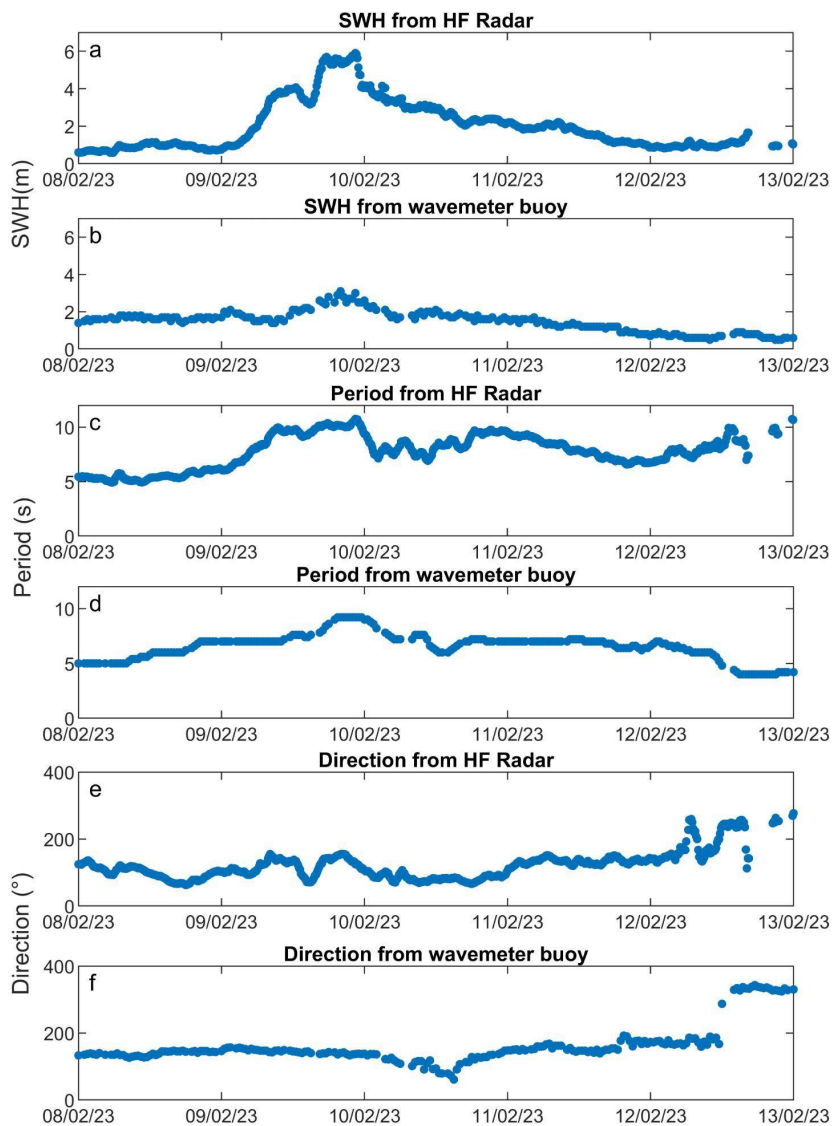
972
973 **Figure 6:** Wave features in terms of SWH, period and mean direction time series retrieved by

974 using the HF Radar (a, c and e) and Mazara del Vallo buoy (b, d and f) data. For the instruments

975 location see **Figure 2c.**
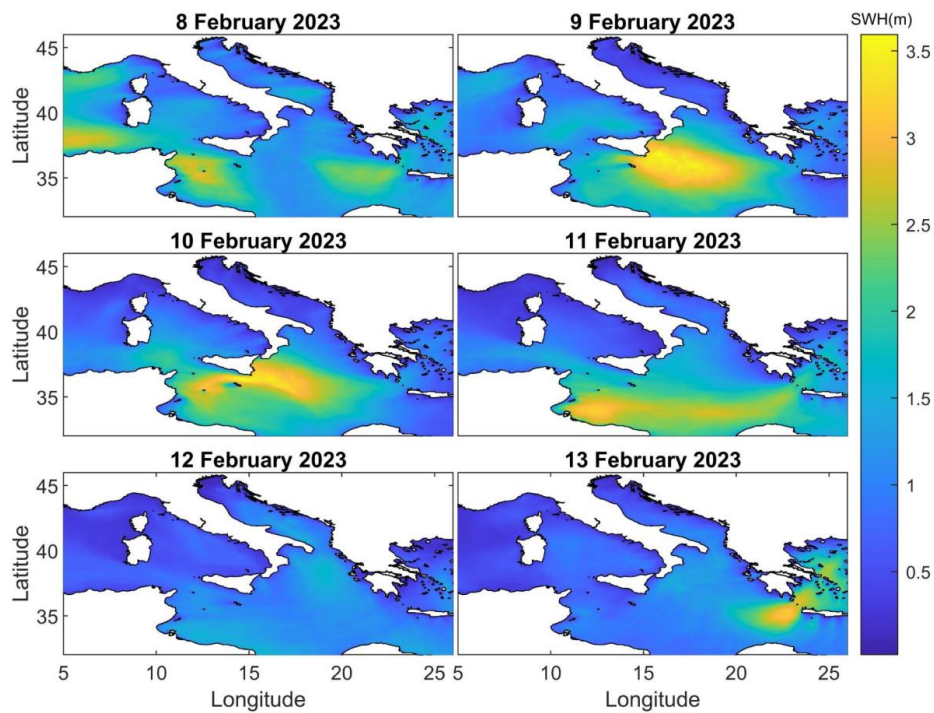
Figure 7: Hindcast maps, obtained from the Copernicus product MEDSEA_HINDCAST_WAV_006_012, showing the spatio-temporal variations of SWH during the days taken into account.
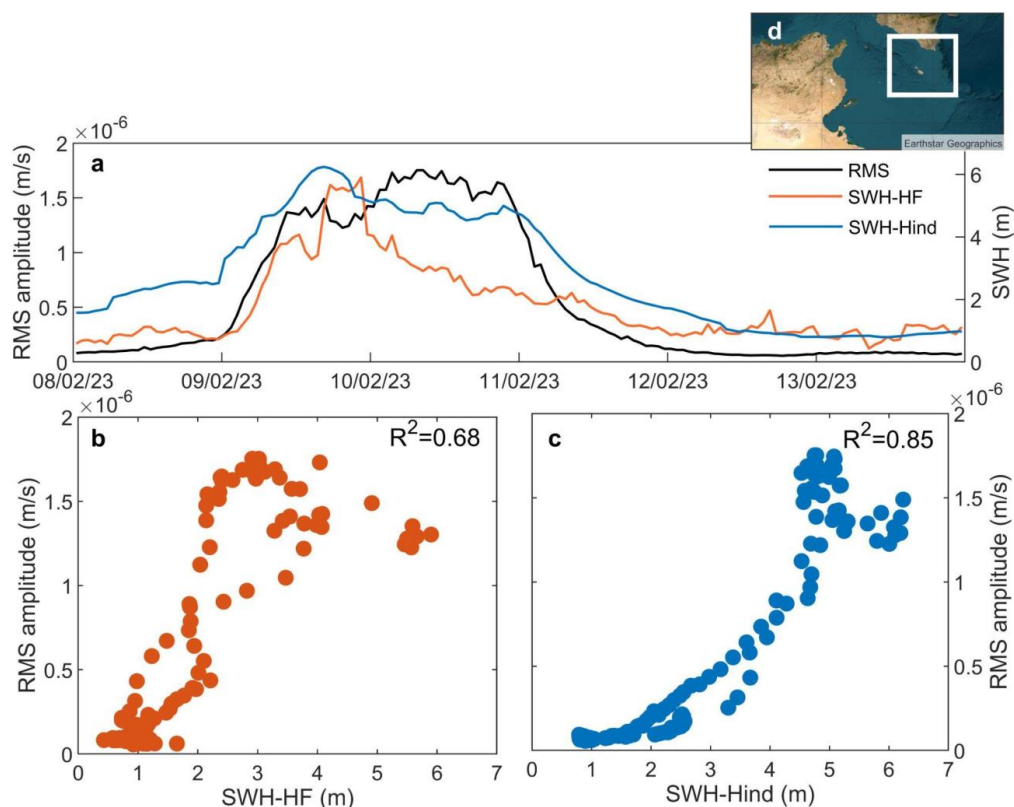
Figure 8: (a) RMS amplitude time series, recorded at the station IWAV5, and SWH time series retrieved by HF Radar (SWH-HF; orange line) and by hindcast data (SWH-Hind; light-blue). Cross-plot showing the relation between SWH-HF and RMS amplitude (b) and between SWH-Hind and RMS amplitude (c). The value of the determination coefficient (R^2) is reported in the upper right corner of the plots (b) and (c). In (d) the area of the Sicily Channel used to calculate the SWH-Hind time series is shown (base image source ©Earthstar Geographic). For the instruments location see **Figure 2a** and **2c**.
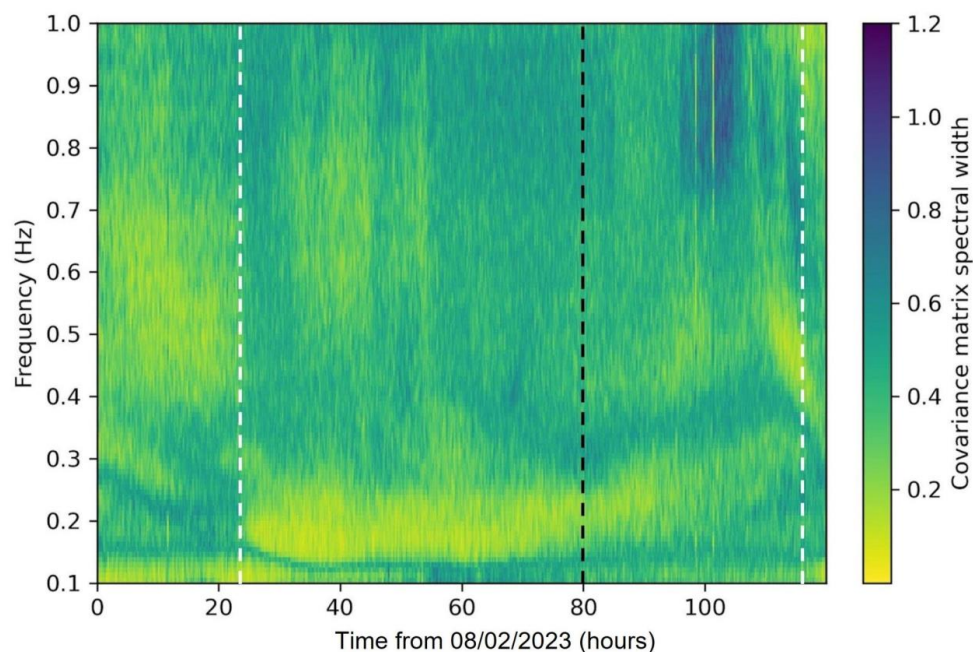
Figure 9: Covariance matrix spectral width obtained for the period 8-12 February 2023 using the stations IWAV5, LINA, MSDA and CLTA. The white dashed lines represent the development and the ending of the sub-tropical system Helios, while the black dashed line indicates the time when Helios makes landfall against the Libyan coast. For stations location see **Figure 2a.**

998   **Table**

Date	Hour	Longitude of microseim source (degrees)	Latitude of microseism source (degrees)	R^2 Value	Longitude of cyclone eye from satellite data (degrees)	Latitude of cyclone eye from satellite data (degrees)
09/02/2023	08:00	15.0000	37.3681	0.3233	/	/
09/02/2023	12:00	15.0000	36.3681	0.3459	/	/
09/02/2023	16:00	15.0000	36.3681	0.3554	/	/
09/02/2023	20:00	15.0000	36.3681	0.3865	/	/
10/02/2023	00:00	14.5000	36.3681	0.4725	/	/
10/02/2023	04:00	14.5000	36.3681	0.5066	14.01584	36.24165
10/02/2023	08:00	14.3030	36.0348	0.5107	13.79612	35.57149
10/02/2023	12:00	14.3030	36.0348	0.5091	13.91697	35.13203
10/02/2023	16:00	14.0000	35.8681	0.4920	13.59836	34.5937
10/02/2023	20:00	14.0000	35.8681	0.4762	13.52146	33.59395
11/02/2023	00:00	14.0000	35.8681	0.3864	13.74118	32.9897

999   **Table 1.** Main features of the microseism sources and comparison with the coordinates of the

1000   cyclone eye retrieved from satellite data. The coordinates of the cyclone eye between 8:00 of

1001   9 Febreuary and 00:00 of 10 February are absent since the cyclone eye is clearly visible

1002   between 01:00 and 23:00 of 10 February 2023.